



CHORUS

This is the accepted manuscript made available via CHORUS. The article has been published as:

Out-of-Contact Elastohydrodynamic Deformation due to Lubrication Forces

Yumo Wang, Charles Dhong, and Joelle Frechette

Phys. Rev. Lett. **115**, 248302 — Published 10 December 2015

DOI: [10.1103/PhysRevLett.115.248302](https://doi.org/10.1103/PhysRevLett.115.248302)

Out-of-contact elasto-hydrodynamic deformation due to lubrication forces

Yumo Wang¹, Charles Dhong¹, and Joelle Frechette^{1,2}

¹Chemical and Biomolecular Engineering Department, and ²Hopkins Extreme Materials Institute

Johns Hopkins University, Baltimore MD 21218.

(Dated November 1, 2015)

Abstract

We characterize the spatiotemporal deformation of an elastic film during the radial drainage of fluid from a narrowing gap. Elastic deformation of the film takes the form of a dimple and prevents full contact to be reached. With thinner elastic film the stress becomes increasingly supported by the underlying rigid substrate and the dimple formation is suppressed, which allows the surfaces to reach full contact. We highlight the lag due to viscoelasticity on the surface profiles, and that for a given fluid film thickness deformation leads to stronger hydrodynamic forces than for rigid surfaces.

PACS numbers: 47.15.G, 68.08.-p, 46.25.-y, 83.50.-v

Surface and interfacial phenomena in soft matter display complex mesoscale behaviors that are qualitatively different from those encountered in stiff materials, such as elastic instabilities during adhesion[1,2] and Schallamach waves in friction[3,4]. Surface [5-7] or viscous[8] stresses can also lead to elastic deformations that are similar to those observed at fluid interfaces. Elastohydrodynamic deformation (EHD), for example, can cause lift and reduce friction during sliding [9-13] and alter the rheological properties of soft colloidal particles[14-17]. Elastohydrodynamic deformation also modifies the shape of approaching surfaces, a determining factor for the adhesion dynamics to wet or flooded surfaces.[18-21] When studying elastohydrodynamics in soft matter it is a challenge to measure simultaneously the hydrodynamic forces and the deformation, both necessary to understand how contact is reached and the coupling between deformation and viscous dissipation.

To illustrate the importance of elastohydrodynamic deformations, consider the normal approach of a rigid sphere toward a surface with an elastically compliant coating in a Newtonian fluid (Fig. 1A). The hydrodynamic forces lead to deformation of the soft material prior to contact ($w(r,t)$), as was visualized by Roberts during the settling of a rubber sphere toward a wall.[8] For elastic half-space this problem can be described by the theory of Davis et al.[22,23] derived for the collision of elastic spheres in fluid, and based on the coupling between lubrication forces and linear elasticity. Recent direct measurements of viscous forces in the presence of a soft surface demonstrated that even minute elastic deformations can have a profound effect on the hydrodynamic interactions.[24,25] Therefore, elasticity likely has to be considered when studying slip at a solid-liquid interfaces. The predominance of soft coatings in tribology and adhesion makes the extension of elastohydrodynamic theory to thin supported films technologically relevant, especially to understand how contact is reached in soft matter. The treatment for supported elastic films, however, is challenging and has limited experimental validation. For thin films (thickness $\ll \sqrt{2Rh}$), the underlying substrate can support a significant fraction of the mechanical stress, which can alter the elastohydrodynamic response from that expected with semi-infinite solids[26,27]. The theory for supported films developed by Charlaix, for instance, elegantly takes advantage of the contribution of the underlying substrate on the hydrodynamic forces to extract the Young's modulus of coatings.[25,27,28] However, the absence of absolute measurement of spatiotemporal separation brings uncertainties to the role played by elasticity on hydrodynamic interactions, especially for the case of thin elastic coatings where our understanding is more limited. Combining visualization of spatiotemporal deformation with force measurements would allow to understand the dynamic of contact formation in soft materials, and to analyze the response of supported films.

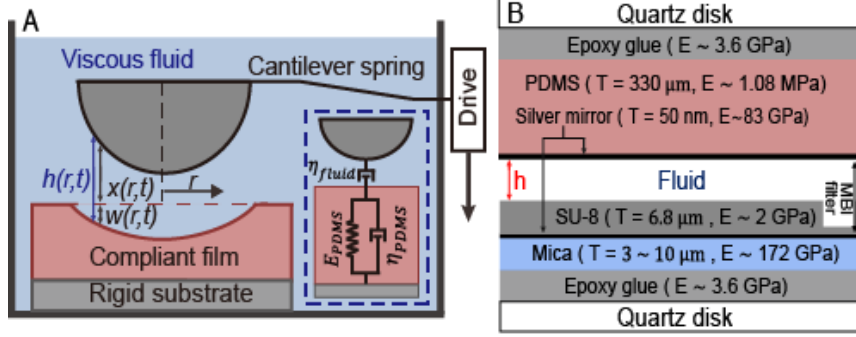


FIG. 1. Schematics (not to scale) of (A) the elastohydrodynamic problem with labelled variables (Inset: Kelvin-Voigt model for elastomer viscoelasticity), and (B) Material layers and properties.

In this letter we investigate the role of compliance on the normal approach of a soft surface toward a rigid one in a viscous Newtonian fluid (Fig. 1A). Spatiotemporal deformation profiles and hydrodynamic forces are measured, and compared to an elastohydrodynamic theory for half-space. We find that elastic deformation in the shape of a dimple at the centerpoint prevents contact between approaching surfaces. We also observe that the finite thickness of the elastic layer restricts the deformation and favors contact. Finally, we show that deformation leads to significantly stronger hydrodynamic forces than those observed with rigid surfaces for the same central separation.

Experiments are performed between crossed-cylinders (equivalent to the sphere-plane geometry) using the Surface Forces Apparatus.[29-31] One surface is rigid (bottom in Fig. 1B) and the other is compliant due to the presence of a relatively thick 330 μm PDMS film (polydimethyl siloxane) coated with a 50 nm silver film as a top layer (top in Fig. 1B). Both surfaces are glued on a cylindrical disk (radius, $R=1.75$ cm). The top silver film facilitates interferometry and prevents swelling in the silicone oil (viscosity, $\eta=0.2\text{Pa}\cdot\text{s}$). An effective Young's modulus of 1.08 ± 0.05 MPa for the PDMS film was obtained by performing *in situ* contact mechanics experiments[32-34] in silicone oil with the same surfaces (see supporting information 2[35-40]). Because of the underlying rigid substrate [41-45], we expect this modulus to overestimate the intrinsic modulus of the PDMS layer by 15-20%.[46,47] We rely on white light multiple-beam interferometry[30,48,49] to map the local fluid film thickness, $h(r,t)$, within nanometer resolution in the normal direction and micron resolution in the lateral direction.

The dynamic experiments follow the approach of Chan and Horn[50,51], where a disk initially at rest and mounted on a cantilever spring (spring constant $k = 165.3$ N/m) is driven toward the other surface at a constant drive velocity (V). The spring deflects because of the drag, and the velocity of the surface (v) is always less than the drive velocity. As the surfaces approach, the hydrodynamic forces increase and deform the PDMS film, as evidenced by the flattening at the center, see III-IV in Fig. 2A. Further

approach lead to an increase in the fluid pressure near the center causing the formation of a dimple in the elastic film, see V-VII in Fig. 2A.

For the theoretical description we employ the lubrication equation in axisymmetric coordinates ($h \ll \sqrt{2Rh}$) and follow closely the treatment of Ref [22] to couple the fluid pressure distribution ($p(r,t)$) with linear elasticity of the compliant film. We treat the elastic film as a half-space in the small strain limit (strain of the PDMS coating here, $\mathcal{E} < 0.5\%$), i.e. we neglect the contribution of the substrate supporting the elastic film. We incorporate a force balance,

$$F(t) = k[h(0,t) - Vt - h(0,0) - w(0,t)] = \int_0^R 2\pi p(r,t) r dr,$$

where the cantilever spring deflects due to the repulsive viscous forces, $F(t)$. Here $h(0,0)$ is the initial separation at the centerpoint. We neglect the radial shear stress on the film and use the no-slip boundary condition for both surfaces. We obtain a solution numerically using the initial fluid film profile ($h(r,0)$) from the experiments as the initial condition without any fitting parameters. As a second description we treat the PDMS film as a viscoelastic material with a viscosity η_{PDMS} , and model the film's response to an applied load as a spring and dashpot in parallel (Kelvin-Voigt model, Fig. 1A). In the viscoelastic description η_{PDMS} is not known *a priori* and we iterate to find a single η_{PDMS} that best describes all the profiles for all drive velocities. (see supporting information [35-40] for details of the model, algorithm, and treatment of viscoelasticity.)

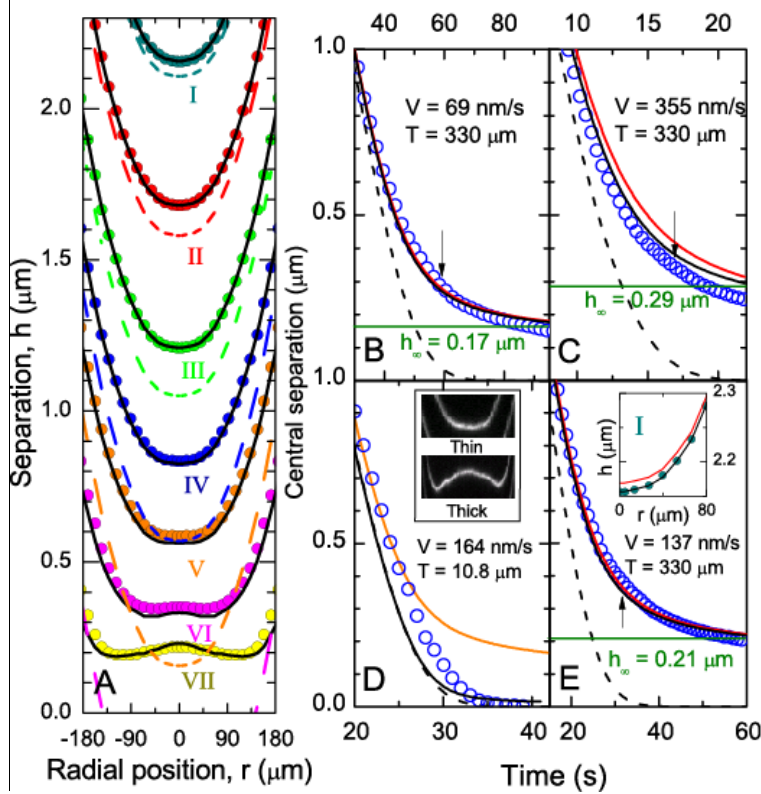


FIG. 2. (A) Experimental and theoretical spatiotemporal surface profile during approach at $V = 137 \text{ nm/s}$. The black solid lines correspond to theoretical predictions treating the PDMS films as a viscoelastic solid. Time stamps are: I: $t = 3.8\text{s}$, II: $t = 8.8\text{s}$, III: $t = 13.8\text{s}$, IV: $t = 18.8\text{s}$, V: $t = 23.8\text{s}$, VI: $t = 33.8\text{s}$, and VII: $t = 53.8\text{s}$. Dash lines are for the positions of the corresponding undeformed sphere. (B-E): Temporal central separation for: (B) $V = 69 \text{ nm/s}$, (C) $V = 355 \text{ nm/s}$, (D) 164 nm/s , and (E) $V = 137 \text{ nm/s}$. (B-C): Effect of drive velocity. (D-E): Effect of film thickness. Black solid lines are the same as in (A), dash lines: Reynolds' theory. Red solid lines are predictions treating the elastomer as an elastic solid. Black arrows: time for dimple formation. h_{∞} : Long time predictions (central $dh/dt < 1\%V$). (D): Approach of a thinner PDMS coating ($T = 10.9 \mu\text{m}$, $R = 1.10\text{cm}$), black rigid line represents predictions for $E = 84 \text{ MPa}$. Yellow line represents the predictions for $E = 1 \text{ MPa}$. Insets of: (D) shape of fringes for thin ($10.9 \mu\text{m}$) and thick ($330 \mu\text{m}$) PDMS film during the approach with $h_{\text{center}} = 150 \text{ nm}$ and (E) Effect of viscosity of PDMS on initial surface profile.

The measured and predicted profiles are shown in Fig. 2. In general the elastic solution is sufficient to describe the surface profile but treating the PDMS as a viscoelastic solid gives a better agreement. The viscoelasticity of the PDMS alters the fluid film profile when the rate of strain is the largest (acceleration and deceleration) such as during start up where viscoelastic contributions are visible (inset of Fig. 2E and supporting information [35-40]). For the viscoelastic predictions, a single value of $\eta_{PDMS} = 1.5 \text{ MPa} \cdot \text{s}$ best fits all the profiles at all velocities, in agreement with literature values.[52] In

Fig. 2A, the predictions with viscoelasticity predict fluid film thicknesses that are always $\pm 35\text{nm}$ of the measured values at the centerpoint. The error increases with drive velocity: at 355nm/s it is $\pm 48\text{nm}$, while it is less than 30nm for 69nm/s . For all drive velocities when the two surfaces are close (strong hydrodynamic forces), the observed separation is less than predicted. This error can be understood considering that surfaces appear stiffer as the forces increase due to the finite thickness of the elastomer, and at a constant time stiffer surfaces are always closer than compliant ones (inset of Fig 4).

Elastic deformation prevents the surfaces from reaching contact at all drive velocities investigated, which is captured by the long time predictions (central $dh/dt < 1\%V$, see Fig. 2B,C,E). As the surfaces approach, flattening away from the centerpoint occurs faster than the normal motion toward the surface, which leads to dramatically large forces and prevents contact. Theoretical solutions for the surface separation are not defined at contact regardless of compliance. For rigid materials, predictions diverge at very short-range where irreversibilities such as roughness, size of fluid molecules, and surface forces often favor contact in experiments[53]. In contrast, for a compliant material, the separation at long times is sufficiently large to prevent these mechanisms from playing a role. With compliant surfaces the drive will lead to a broader surface instead of significantly decreasing the central fluid film thickness, at least until non-linear effects occur. Note that contact can be reached under quasi-static condition.

The thickness of the compliant layer plays an important role in determining the spatiotemporal fluid film thickness. We contrast the temporal change in surface separation at the centerpoint of a thick ($T=330\ \mu\text{m}$, Fig. 2E) and thin ($T=10.9\ \mu\text{m}$, Fig. 2D) PDMS films for similar drive velocities. Both films have the same bulk mechanical properties, however the effective modulus is much larger ($E=84\ \text{MPa}$) for the thin film because of incompressibility and apparent stiffening due to the underlying rigid substrate (supporting information[35-40])[54,55]. For the thin film, as the hydrodynamic forces increase, the stress becomes increasingly supported by the rigid substrate. As a result, the temporal fluid film thickness gradually transitions from being the one predicted for a compliant material ($E=1\text{MPa}$) to that of a rigid one (see predictions for the two moduli in Fig. 2D). We find that the effective stiffening suppresses the formation of a dimple (within our spatial resolution) in the elastic film, and that contact can be reached in a fashion similar than for rigid materials. Such a transition to a rigid-like behavior is not observed with the thicker film. This stiffening effect is well-characterized for contact mechanics experiments[45]. Our work shows how the finite thickness of the elastic film gradually alters the deformation profile from that of a semi-infinite compliant material as the surfaces approach and how it favors contact. Increasing the modulus in the model will not give better agreement with experiments, and always make the far-field predictions significantly worse (see supporting information[35-40]). An alternative treatment would be to use a solution for arbitrary axisymmetric pressure distribution for a finite thickness elastic layer, such as

in Refs [26,27], to obtain a solution valid at all h . A simplified scaling argument treating the deformation solely as shear, such as in Ref [27] could also work close to contact but not for the far-field. The importance of film thickness on the force required to make contact has profound implications for hydrodynamic interactions with soft materials and coatings, such as in biological systems, tribology, adhesion, and rheology.

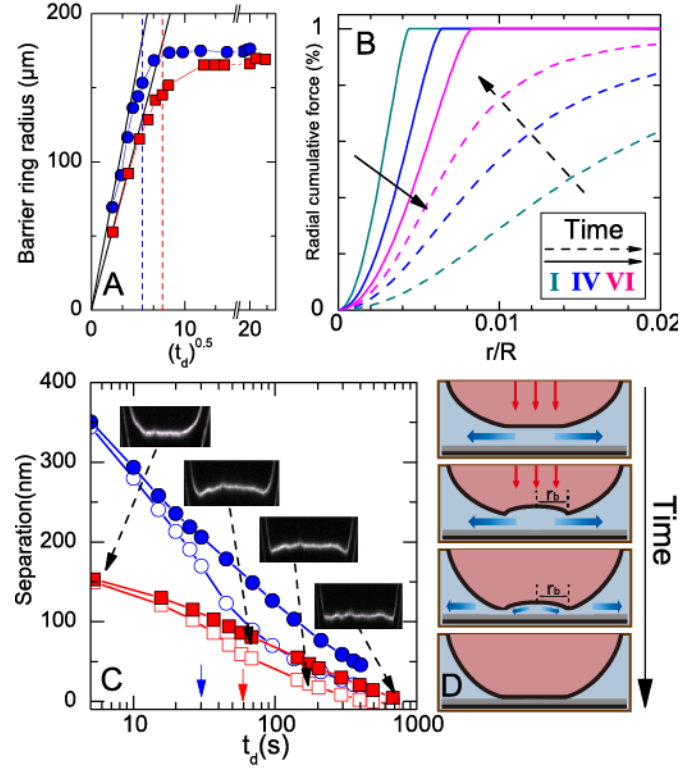


FIG. 3. (A) Growth of barrier ring radius (r_b). Squares: $V = 69$ nm/s, circles: $V = 137$ nm/s. t_d (s) is the time elapsed after center curvature of the elastomer becomes negative. Black solid lines: $r_b = \sqrt{RV\Delta t / 2}$. Vertical dashed lines indicate when the motor stopped. (B) Radial cumulative force (%) as a function of r/R for $V = 137$ nm/s. The roman numerals represent the same times as those of Fig. 2A. Solid lines correspond to the relative cumulative force results from a spherical indenter with the same load as that in EHD (Dashed lines), calculated from Hertz contact mechanics. (C) Centerpoint (solid) and edge (open) separation after dimple formation (circles: $V=137$ nm/s, squares: $V=69$ nm/s). Inset: Corresponding interference fringes for $V = 69$ nm/s. Solid arrows: motor stop time for $V = 137$ nm/s and $V = 69$ nm/s. (D) Schematic showing formation and relaxation of dimples with a barrier ring r_b .

The formation of dimple—a bell of liquid trapped around the centerpoint—is observed as the force increases (Fig. 2A). Once formed ($t_d=0$) the growth of dimples forming a barrier ring r_b follows the same geometric scaling as the one observed for fluid droplets, and is independent of materials properties ($r_b = \sqrt{RV\Delta/2}$, Fig. 3A)[56,57]. This scaling implies that beyond t_d the fluid film thickness remains essentially constant while the increase in pressure is almost solely accommodated by elastic deformation. The appearance of a dimple requires the fluid pressure to be highly concentrated near the centerpoint and our model (Fig. 3B) shows that as the force increases, the fluid pressure distribution becomes increasingly more concentrated near the center. We compare the radial cumulative force with the one predicted based on a Hertzian contact for the same force (Fig. 3B). For a given force, a spherical indenter always leads to a narrower pressure distribution than the elastohydrodynamic case. As the force increases, however, the contact area based on indentation increases while the elastohydrodynamic pressure distribution becomes shaper and significantly more concentrated near the centerpoint (compare the radial cumulative force at the Hertz contact radius for the three cases shown in Fig. 3B).

If we stop the motor (near the limit of the range of the motor), the surface velocity decreases but does not stop because of the stored energy in the cantilever. The dimple slowly relaxes after the motor stops (see Fig. 3C), and after a long time contact can be reached first at the edge of the ring, followed later by near contact (to within 10nm) at the centerpoint (Fig. 3C). This process is very slow ($\gg 100s$): the fluid has to drain through the edge of the dimple as the pressure drop between the center and the surrounding decreases. During this relaxation a fluid pocket can be trapped at the center while contact is reached at the edge.

The measured hydrodynamic forces and predictions for soft and rigid surfaces are shown in Fig. 4. The experimental points are calculated based on the measured fluid film profile and predictions for the model treat the PDMS film as a viscoelastic solid. To calculate the hydrodynamic force from our experimental data we used the prediction for w at the centerpoint (see supporting information [35-40]). In general our experiments show excellent agreement with predictions over all the velocities, with the largest error present for the fastest drive velocity and close to contact. When comparing the hydrodynamic forces between soft and rigid surfaces we see that predictions based on rigid surfaces underestimate the real force for all fluid film thicknesses. In contrast, Reynolds theory always overestimates the force at a given time (inset of Fig. 4). For a given fluid film thickness the deformed surface is flatter, giving rise to larger hydrodynamic repulsion than for rigid surfaces. In contrast, at a given time t rigid surfaces are always closer to contact and the force is higher than for a deformable surface. We also observe systematic deviation in the hydrodynamic forces at small h and at long times that are attributed to the effective

stiffening caused by the rigid underlying substrate. If we compare with AFM experiments where only $F(t)$ and $x(r,t)$ are known, predictions based on Reynolds theory would overestimate the measured force: for the same $x(r,t)$ a rigid surface has a smaller separation (h) than the compliant surface. Thus the rigid case predicts a larger force than measured because of the different h , as shown by Ref [24].

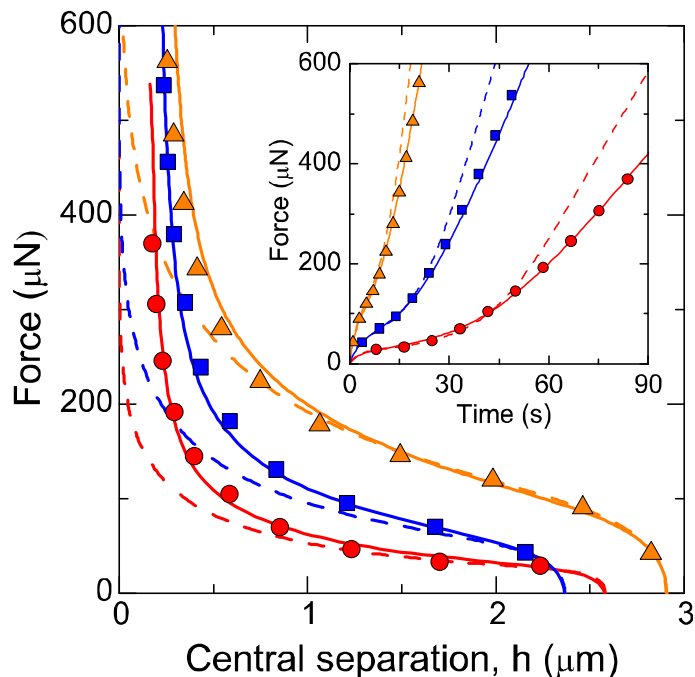


FIG. 4. Repulsive elastohydrodynamic force as a function of central separation, h . Circles: $V = 69$ nm/s, squares: $V = 137$ nm/s, triangles: $V = 355$ nm/s. Dash lines: predictions for rigid surfaces, solid lines: predictions for compliant surfaces treating the elastomer as a viscoelastic solid. Inset: corresponding force as a function of time.

In summary, we characterized the spatiotemporal deformation of a compliant film during the normal drainage of fluid from a narrowing gap. For a thick elastic film (approx. half-space) we observe that elastic deformation in the form of a dimple prevents the surfaces from reaching contact. For a thinner elastic the formation of the dimple is suppressed and contact can be reached because the stress is supported by the underlying substrate. We find that the growth of the dimples in the elastic films is nearly independent of the mechanical properties of the film. Finally we find that at a given time elastic compliance leads to weaker forces while it leads to stronger forces at a given fluid film thickness. Measuring absolute surface separation is critical when working with soft materials, such as in biological systems or in the lubrication of surfaces with compliant coatings of a finite thickness.

Acknowledgements. This work is partially supported by the Office of Naval Research – Young Investigator Award (N000141110629), by the Donors of the American Chemical Society Petroleum

Research Fund under Grant 51803-ND5, the Hopkins Extreme Materials Institute (HEMI), and NSF-CMMI 1538003.

References.

- [1] A. Ghatak and M. K. Chaudhury, *J. Adhes.* **83**, 679 (2007).
- [2] S. Yang, K. Khare, and P. C. Lin, *Adv. Funct. Mater.* **20**, 2550 (2010).
- [3] C. J. Rand and A. J. Crosby, *J. Appl. Phys.* **106**, 4, 064913 (2009).
- [4] K. Vorvolakos and M. K. Chaudhury, *Langmuir* **19**, 6778 (2003).
- [5] J. S. Wexler, T. M. Heard, and H. A. Stone, *Phys. Rev. Lett.* **112**, 5, 066102 (2014).
- [6] L. A. Lubbers, J. H. Weijs, L. Botto, S. Das, B. Andreotti, and J. H. Snoeijer, *J. Fluid Mech.* **747**, 12, R1 (2014).
- [7] R. W. Style, R. Boltyanskiy, Y. L. Che, J. S. Wettlaufer, L. A. Wilen, and E. R. Dufresne, *Phys. Rev. Lett.* **110**, 5, 066103 (2013).
- [8] A. Roberts, *J. Phys. D: Appl. Phys.* **4**, 423 (1971).
- [9] D. Dowson, *Wear* **190**, 125 (1995).
- [10] A. Gopinath and L. Mahadevan, in *Proceedings of the Royal Society of London A: Mathematical, Physical and Engineering Sciences* (The Royal Society, 2011), p. rspa20100228.
- [11] J. M. Skotheim and L. Mahadevan, *Phys. Fluids* **17**, 092101 (2005).
- [12] M. Scaraggi, G. Carbone, B. N. J. Persson, and D. Dini, *Soft Matter* **7**, 10395 (2011).
- [13] G. A. Ateshian, H. Wang, and W. M. Lai, *J. Tribol.* **120**, 241 (1998).
- [14] J. R. Seth, L. Mohan, C. Locatelli-Champagne, M. Cloitre, and R. T. Bonnecaze, *Nat. Mater.* **10**, 838 (2011).
- [15] A. Ikeda, L. Berthier, and P. Sollich, *Phys. Rev. Lett.* **109**, 018301 (2012).
- [16] M. Gross, T. Kruger, and F. Varnik, *Soft Matter* **10**, 4360 (2014).
- [17] S. Adams, W. Frith, and J. Stokes, *J. Rheol.* (1978-present) **48**, 1195 (2004).
- [18] J. Iturri, L. Xue, M. Kappl, L. García - Fernández, W. J. P. Barnes, H. J. Butt, and A. del Campo, *Adv. Funct. Mater.* (2015).
- [19] B. N. J. Persson, *J. Phys. Condens. Matter* **19**, 16, 376110 (2007).
- [20] L. Heepe and S. N. Gorb, *Annu. Rev. Mater. Res.* **44**, 173 (2014).
- [21] C. Dhong and J. Frechette, *Soft Matter* **11**, 1901 (2015).
- [22] R. H. Davis, J.-M. Serayssol, and E. Hinch, *J. Fluid Mech.* **163**, 479 (1986).
- [23] G. Barnocky and R. H. Davis, *Phys. Fluids* **31**, 1324 (1988).
- [24] F. Kaveh, J. Ally, M. Kappl, and H. J. Butt, *Langmuir* **30**, 11619 (2014).
- [25] S. Leroy, A. Steinberger, C. Cottin-Bizonne, F. Restagno, L. Leger, and E. Charlaix, *Phys. Rev. Lett.* **108**, 264501 (2012).
- [26] X. Zhao and R. Rajapakse, *Int. J. Eng. Sci.* **47**, 1433 (2009).
- [27] S. Leroy and E. Charlaix, *J. Fluid Mech.* **674**, 389 (2011).
- [28] R. Villey, E. Martinot, C. Cottin-Bizonne, M. Phaner-Goutorbe, L. Léger, F. Restagno, and E. Charlaix, *Phys. Rev. Lett.* **111**, 215701 (2013).
- [29] D. Tabor and R. H. S. Winterton, *Proc. R. Soc. London, Ser: A* **312**, 435 (1969).
- [30] J. N. Israelachvili, *J. Colloid Interface Sci.* **44**, 259 (1973).
- [31] J. N. Israelachvili *et al.*, *Rep. Prog. Phys.* **73**, 036601 (2010).
- [32] K. L. Johnson, K. Kendall, and A. D. Roberts, *Proc. R. Soc. London, Ser. A* **324**, 301 (1971).
- [33] M. K. Chaudhury and G. M. Whitesides, *Science* **255**, 1230 (1992).
- [34] K. Khanafer, A. Duprey, M. Schlicht, and R. Berguer, *Biomed. Microdevices* **11**, 503 (2009).
- [35] For PDMS preparation, calculation of the effective modulus and layering effect, determination of the deformation and numerical algorithm, see Supplemental Material, which include Refs.[36-40].

- [36] J. N. Lee, C. Park, and G. M. Whitesides, *Anal. Chem.* **75**, 6544 (2003).
- [37] M. Heuberger, *Rev. Sci. Instrum.* **72**, 1700 (2001).
- [38] G. Lian, M. J. Adams, and C. Thornton, *J. Fluid Mech.* **311**, 141 (1996).
- [39] J.-M. S  rayssol, *Dynamic deformation and rebound of particles during filtration and coagulation*, University of Colorado, 1985.
- [40] B. Hughes and L. White, *Q. J. Mech. Appl. Math.* **32**, 445 (1979).
- [41] I. Sridhar, K. L. Johnson, and N. A. Fleck, *J. Phys. D: Appl. Phys.* **30**, 1710 (1997).
- [42] K. L. Johnson and I. Sridhar, *J. Phys. D: Appl. Phys.* **34**, 683 (2001).
- [43] P. M. McGuiggan, J. S. Wallace, D. T. Smith, I. Sridhar, Z. W. Zheng, and K. L. Johnson, *J. Phys. D: Appl. Phys.* **40**, 5984 (2007).
- [44] F. K. Yang, W. Zhang, Y. G. Han, S. Yoffe, Y. C. Cho, and B. X. Zhao, *Langmuir* **28**, 9562 (2012).
- [45] E. Barthel and A. Perriot, *J. Phys. D: Appl. Phys.* **40**, 1059 (2007).
- [46] K. R. Shull, *Mater. Sci. Eng. R-Rep.* **36**, 1 (2002).
- [47] E. K. Dimitriadis, F. Horkay, J. Maresca, B. Kachar, and R. S. Chadwick, *Biophys. J.* **82**, 2798 (2002).
- [48] S. Tolansky, *Multiple-Beam Interferometry of surfaces and films* (Oxford University Press, London, 1948).
- [49] R. Gupta and J. Fr  chette, *J. Colloid Interface Sci.* **412**, 82 (2013).
- [50] D. Y. C. Chan and R. G. Horn, *J. Chem. Phys.* **10**, 5311 (1985).
- [51] R. Gupta and J. Fr  chette, *Langmuir* **28**, 14703 (2012).
- [52] S. T. Choi, S. J. Jeong, and Y. Y. Earmme, *Scr. Mater.* **58**, 199 (2008).
- [53] R. Horn and J. Israelachvili, *Macromolecules* **21**, 2836 (1988).
- [54] A. Perriot and E. Barthel, *J. Mater. Res.* **19**, 600 (2004).
- [55] E. Barthel, A. Perriot, A. Chateauminois, and C. Fretigny, *Philos. Mag.* **86**, 5359 (2006).
- [56] J. N. Connor and R. G. Horn, *Farad. Discuss.* **123**, 193 (2003).
- [57] R. Manica, J. N. Connor, S. L. Carnie, R. G. Horn, and D. Y. C. Chan, *Langmuir* **23**, 626 (2007).